RESEARCH ARTICLE | JANUARY 06 2025

Interpretation and prediction of the three-dimensional coherent structure and its dynamics of tornado-like vortex via delayed proper orthogonal decomposition

Lei Zhou (周蕾) ; Bernd R. Noack ; Kam Tim Tse (谢锦添) ; Xuhui He (何旭辉)

Physics of Fluids 37, 013106 (2025)
https://doi.org/10.1063/5.0234437

Physics of Fluids ARTICLE pubs.aip.org/aip/pof

Interpretation and prediction of the three-dimensional coherent structure and its dynamics of tornado-like vortex via delayed proper orthogonal decomposition

Cite as: Phys. Fluids **37**, 013106 (2025); doi: 10.1063/5.0234437
Submitted: 21 August 2024 · Accepted: 25 November 2024 ·
Published Online: 6 January 2025

View Online Export Citation CrossMark

Lei Zhou (周蕾),[1,2] Bernd R. Noack,[3,4] Kam Tim Tse (谢锦添),[5] and Xuhui He (何旭辉)[1,a)]

AFFILIATIONS

[1]School of Civil Engineering, Central South University, Changsha 410083, China
[2]Department of Civil and Environment Engineering, Hong Kong Polytechnic University, Hong Kong, China
[3]Chair of Artificial Intelligence and Aerodynamics, School of Mechanical Engineering and Automation, Harbin Institute of Technology, Shenzhen 518055, China
[4]Guangdong Provincial Key Laboratory of Intelligent Morphing Mechanisms and Adaptive Robotics, Harbin Institute of Technology, Shenzhen 518055, China
[5]Department of Civil and Environmental Engineering, The Hong Kong University of Science and Technology, Clear Water Bay, Kowloon, Hong Kong, China

[a)]**Author to whom correspondence should be addressed:** xuhuihe@csu.edu.cn

ABSTRACT

This study proposes a three-dimensional mode-based surrogate framework to predict the tornado-like vortex (TLV) derived from the fuzzy neural network and delayed proper orthogonal decomposition method. First, near-break-down TLV is simulated via large-eddy simulation, and its mean, fluctuating and statistical flow feature is analyzed. Then, three-dimensional spatiotemporal features of coherent structure are extracted and interpreted. Next, the capability of the proposed framework to predict the future state of an unsteady chaotic TLV flow field is systematically evaluated, including the spatiotemporal variation of velocity, pressure, and vorticities as well as flow statistics. Finally, parametric analysis is also conducted to investigate the influence of three key parameters [i.e., Fuzzy rules of the state network or output network (*K1* or *K2*), time delayed embedding number (*d*)] contained in the framework and the step number of forward prediction (*K*) on the predicted accuracy. Results show that for near-break-down TLV, vortex wandering effect largely affects its dynamical feature, and its three-dimensional characteristics are distinct, exhibiting the essence of the swirling jet flow. 3D mode-based surrogate model can correctly predict the tornado-like vortex with a relative error of less than 2% for the radial, tangential, and vertical velocity component. It is found that fuzzy rules and time-delayed embedding number has great effect on prediction accuracy. Thus, to achieve optimal predicting effect, it is suggested that *d* is taken as 8, *K1*, and *K2* are taken as 18, and when making multi-step predictions, the largest *K* should not exceed 7.

I. INTRODUCTION

Tornadoes are destructive extreme weather events that have become more frequent and intense globally, causing significant structural damage, economic losses, and human casualties (Rodríguez *et al.*, 2021; Tochimoto, 2022). Understanding the mechanisms governing their formation, evolution, and associated tornadic loads is a challenging research area. Tornadoes have complex three-dimensional wind fields with substantial radial, tangential, and axial velocity components, which differ significantly from synoptic winds (Davies-Jones, 2015; Gunár *et al.*, 2023; and Honerkamp *et al.*, 2020). The sudden onset, short duration, and rapid propagation of tornadoes pose significant challenges for current wind field data acquisition techniques with limited temporal resolution and spatial range (Honerkamp *et al.*, 2020; Womble *et al.*, 2018).

Analytical models, experimental, and numerical vortex simulators have emerged as viable alternatives to measuring real tornado fields (Chen and Lombardo, 2019; Gairola and Bitsuamlak, 2019; and Refan and Hangan, 2018). While analytical models are useful for efficient

tornado design and risk assessment, they do not account for the intricate flow and turbulence phenomena present in tornado vortices (Gillmeier *et al.*, 2018; Romanic *et al.*, 2016; and Standohar-Alfano *et al.*, 2017). Tornado-like vortex generators, including Ward-type and ISU-type, are commonly used to investigate wind loads on structures and equipment caused by tornadoes (Haan Jr., *et al.*, 2008; Ward, 1972). However, only a limited number of research institutions possess this advanced experimental apparatus. Table I summarizes the key parameters of existing laboratory tornado-like vortex generators worldwide. Numerical tornado-like vortex generators, on the other hand, are widely used due to their low computational cost, adjustable geometric parameters, and high calculation accuracy for evaluating three-dimensional tornadic flow fields and tornado-induced wind responses (Huo *et al.*, 2020; Wang *et al.*, 2022; Xu *et al.*, 2017; and Zhang *et al.*, 2024).

Despite differences in their size and type of vortex chamber, tornado simulators generate similar tornado-like flow patterns, and the variation of these structures with key influencing parameters, such as vortex ratio, is also akin (Liu and Ishihara, 2015; Verma and Selvam, 2021). This indicates that vortex simulators can accurately reproduce essential characteristics of a tornado, including both the mean and dominant turbulent flow features represented by coherent structures (Ashrafi *et al.*, 2021; Gairola and Bitsuamlak, 2019). However, there is limited understanding of the underlying physics of fluctuating turbulent flow features with more emphasis on mean tornadic flow characteristics (Baker and Sterling, 2019; Tang *et al.*, 2018). To accurately assess, predict, and manage tornado-induced disasters, it is crucial to understand the fundamental dynamics of tornadic flow, with a particular focus on its coherent structures (Karami *et al.*, 2020; Wang *et al.*, 2021).

Data-driven pattern decomposition methods are powerful and efficacious tools for detecting and extracting coherent structures in wind engineering and fluid mechanics (Begiashvili *et al.*, 2023; Li *et al.*, 2023). Although they have exhibited admirable performance in uniform wind, atmospheric boundary layer wind, and twisted wind scenarios, there is scarce research on their use for tornado-like vortex pattern extraction. Recently, Karami *et al.* (2019) compared the coherent structure and dynamic characteristics of tornado-like vortices under different swirling ratios. They proposed a simplified large-scale and low-order turbulence model for generating tornado vortex structure. Zhang *et al.* (2023) proposed a new unified wind spectrum formula for a single-cell tornado-like vortex based on the relationship between the coherent structure captured by proper orthogonal decomposition (POD) and the fluctuating velocity. However, these studies only focused on the coherent structure on the two-dimensional planes, which cannot represent the complexity of the 3D tornado vortex given the natural existence of the non-axial symmetry and large axial velocity component. Thus, investigating the three-dimensional coherent structure of tornadoes is imperative for providing a precise depiction of their shape and motion, particularly the intricate variations in the vertical direction. This will bolster the accuracy of tornado development prediction and control.

Directly predicting high-dimensional and nonlinear full-order complex flow fields is a computationally demanding task, whether it is the solution of the Navier–Stokes equation or the training of machine learning models. Developing hybrid data-driven reduced order modeling (ROM) models is a promising and efficient alternative approach (Buccino, 2022; Raj *et al.*, 2023; and Zancanaro *et al.*, 2022). By identifying the low-order representation of high-dimensional flow fields, the dynamic system can be accurately learned, and the time series of flow fields can be effectively predicted (Zhu *et al.*, 2024b; Zhu *et al.*, 2024c). Proper orthogonal decomposition (POD) is a widely adopted projection-based technique for fluid flow reduction modeling (Mendez *et al.*, 2019; Ooi *et al.*, 2021; and Wu *et al.*, 2019). Delayed-POD (d-POD) is an advanced variant of POD that utilizes Taken's embedding theory to reconstruct dynamics through time-delayed embedding, leading to smoother mode coefficients and enhanced intrinsic characteristics (Zhou *et al.*, 2023). The crux of using a reduced-order model based on POD for complex flow field prediction is to extract and accurately predict the primary mode coefficients, which can be regarded as chaotic time series. In terms of chaotic time series prediction methods, the recursive fuzzy neural network (RFNN) has received extensive attention due to its ability to integrate the potential of RNN in learning time dependencies with FNN's ability to handle fuzzy information, leading to satisfactory predictive performance (Ding *et al.*, 2021; Luo *et al.*, 2019). However, traditional RFNN may have limitations when dealing with chaotic time series, because they can usually only learn a single function, and chaotic systems may produce different outputs

TABLE I. Summary of the key parameters of existing laboratory tornado-like vortex generators.

Institute (wind tunnel name)	Type	Swirl ratio	Radius of test region (m)	Radius of vortex core (m)	Maximum tangential velocity (m/s)
TJ (TJ-6)	ISU-type	0.72	1.5	0.1	12
BJTU	ISU-type	0.72	1.5	0.11	12
WUST	∼	0.8	1.5	0.1	15
CSU (CSU-WT5)	Ward-type	2	12	2	30
CQU	∼	0.1–1	1.5	0.1	15
UWO (WindEEE Dome)	Ward-type	1.03	5	∼	16
TTU (VorTEC)	Ward-type	0–2.2	10.2	0.52	13.3
ISU (ISU)	ISU-type	0.08–1.14	5.49	0.56	14.5
UoB	Ward-type	0.69	3.6	0.31	8.8
MSU	ISU-type	∼	2.1	∼	∼
Meijo Univ.	ISU-type	0.4–1.8	0.8	0.1	8

under the same input, depending on the state. To address this issue, the multi-functional recurrent fuzzy neural network (MFRFNN) has been developed (Nasiri and Ebadzadeh, 2022; Zhang *et al.*, 2024). MFRFNN incorporates multiple states for learning multiple functions simultaneously, enabling the capture of dynamic characteristics of the chaotic time series and the prediction of long-term values. While MFRFNN cannot be directly applied to learn high-dimensional complex flow fields from full-order data, it holds great potential in predicting reduced-order models of complex flow fields. Therefore, it is imperative to assess the applicability and effectiveness of MFRFNN in predicting POD mode coefficients, which, to the best of the authors' knowledge, has not been investigated in the literature.

Contemporary research in the field of tornadoes has primarily centered on qualitative flow visualization and the quantitative depiction of mean flow, while disregarding the precise portrayal of the three-dimensional attributes of tornadoes, such as spatial coherent structures and temporal evolutionary patterns (Refan and Hangan, 2016; Wang *et al.*, 2017). Moreover, the inadequate comprehension of the three-dimensional space-time characteristics analogous to tornadoes has impeded the precise prediction of tornado-like wind fields (Cao and Liu, 2023; Sobash *et al.*, 2016). Thus, there is strong motivation to (i) understand the associated 3D vortex dynamics, which may be responsible for extreme negative pressures and therefore damage and (ii) to develop a 3D mode-based tornado field prediction neural network to obtain an accurate prediction in the tornado prevention analysis application. To this end, this study, the three-dimensional flow field of near-break-down tornado-like vortex was conducted using large eddy simulation (LES). A novel 3D mode-based recursive fuzzy prediction framework based on the combination of d-POD and MFRFNN was proposed to extract 3D mode spatial-temporal feature and predict the three-dimensional tornadic flow field. The efficacy of this newly proposed prediction model was systematically evaluated; then, parametric analysis was conducted.

II. NUMERICAL SIMULATION OF TORNADO VORTEX

A. Governing equation and solution scheme

The generation of a tornado-like vortex is achieved through large eddy simulation. This method involves applying a spatial filter to the flow field and retaining the low-frequency components, while modeling the remaining small eddies using sub-grid scale (SGS) models. The large eddy is directly solved. The Smagorinsky–Lilly model is utilized to calculate the SGS stress in this simulation. The filtered NS equations for the incompressible flow can be expressed accordingly,

$$\frac{\partial \widetilde{u}_i}{\partial x_i} = 0, \tag{1a}$$

$$\frac{\partial \widetilde{u}_i}{\partial t} + \frac{\partial \widetilde{u}_i \widetilde{u}_j}{\partial x_j} = \frac{\partial}{\partial x_j}\left(\nu \frac{\partial \widetilde{u}_i}{\partial x_j}\right) - \frac{\partial \widetilde{p}}{\partial x_i} - \frac{\partial \tau_{ij}}{\partial x_j}, \tag{1b}$$

where $\tilde{u}_i$ is the filtered velocity, v is the viscosity, and τ_{ij} is the SGS stress expressed as follows:

$$\tau_{ij} = -2\nu_t \widetilde{S}_{ij} + \frac{1}{3}\tau_{kk}\delta_{ij}, \quad \widetilde{S}_{ij} = \frac{1}{2}\left(\frac{\partial \widetilde{u}_i}{\partial x_j} + \frac{\partial \widetilde{u}_j}{\partial x_i}\right), \tag{2a}$$

where SGS turbulent viscosity, ν_t, is parameterized by the static Smagorinsky–Lilly model, while the Kronecker delta, δ_{ij}, is equal to 1 when $i = j$, and 0 when $i \neq j$. The Smagorinsky–Lilly model is used for the SGS turbulent viscosity expressed by

$$\nu_t = L_s^2 \sqrt{2\widetilde{S}_{ij}\widetilde{S}_{ij}}, \quad L_s = \min(\kappa d, C_s V^{1/3}), \tag{2b}$$

where L_s denotes the mixing length for subgrid-scales, κ is the von Karman constant, i.e., 0.42, d is the distance to the closest wall and V is the volume of a computational cell. Here, C_s is the Smagorinsky constant, which is determined to be 0.032.

The finite volume method (FVM) is employed to solve the problem, with the second-order central difference scheme used for the convective and viscous terms, and the second-order implicit scheme used for the unsteady term. The discretized equations are solved using the semi-implicit pressure linked equations (SIMPLE) algorithm, implemented in the commercial solver ANSYS Fluent. To ensure that the Courant Friedrichs Lewy (CFL) number does not exceed 1 in the entire computational domain, the time step Δt is set to 10^{-5} s.

B. Computational domain and boundary condition

The present study simulates a tornado-like vortex (TLV) with a swirl ratio S of 0.35 in the Ward-type simulator. The swirl ratio is calculated by $S = \frac{\tan\theta}{2a}$, where θ is the inflow angle of 55°, $a = h_g/r_o$, h_g is the height of the convergence region of 0.2 m, and r_o is the radius of the updraft hole of 0.25 m. The computational domain has the same configuration and dimensionality as that in Liu and Ishihara (2015), which is 1/1900 of the physical simulator size used in the previous experimental study (Matsui and Tamura, 2009). The detailed parameters of the computational domain are presented in Fig. 1. The boundary conditions at the top of the exhaust region are set as the Dirichlet boundary condition, while the side of the convergence region is set as the Neumann boundary condition, with the inlet velocity component profiles specified accordingly

$$\begin{cases} U_{rg} = U_1 \left(\dfrac{z}{z_1}\right)^{1/n}, \\ V_{rg} = -U_{rg}\tan(\theta), \end{cases} \tag{3}$$

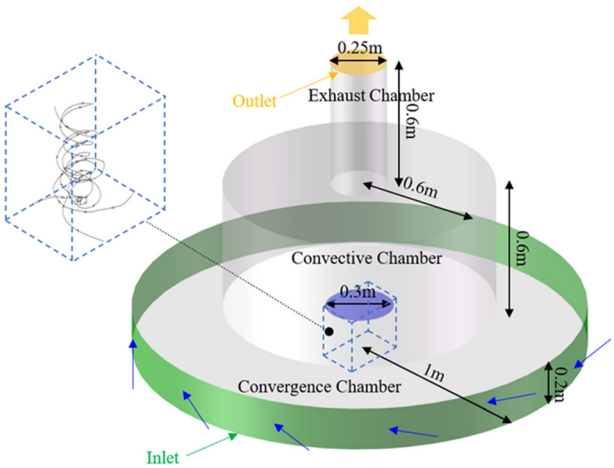

FIG. 1. Computational domain and boundary condition of the numerical simulation.

where the radial and tangential velocities are denoted by U_{rg} and V_{rg}, respectively. U_1 represents the reference radial velocity at the reference height z_1, which is set to be 0.024 m/s and 0.01 m, respectively. The parameter n is equal to 1/7. For the ground, the boundary condition no-slip wall is adopted. Here, to resolve the fluid dynamics, the wall function is not adopted for the wall boundary conditions. The maximum value of dimensionless wall distance yplus is less than 1.0, and the growth rate is less than 1.1.

C. Mesh scheme and numerical results verification

Considering the axisymmetric nature of tornado-like vortices, an axisymmetric grid is adopted, as displayed in Fig. 2. The lateral view of the mesh is depicted in Fig. 2(a). The smallest grid size in the radial direction is 0.1 mm, and the growth rate is less than 1.1 from the center to the outside. In the vertical direction, the minimum grid size near the bottom is 0.05 mm, and a growth rate of less than 1.1 is employed. The nondimensional distance between the grid center of the first layer and the wall (y^+) is less than 1. The total number of grids is about 7.6×10^6. To verify grid independence, a coarser mesh with a grid number of 3.4×10^6 and a finer mesh with a grid number of 9.5×10^6 are generated. The numerical results of the three meshes are in close agreement with each other and with the experiment reported by Matsui and Tamura (2009), indicating that the results are grid independent. Therefore, the medium mesh, whose grid number is higher than that of Liu and Ishihara (2015), is used to carry out the simulation in this study.

To normalize the flow fields, the maximum tangential velocity in the cyclostrophic balance region, V_c, is used in the subsequent discussion. Additionally, the radial distance is normalized by the core radius of the tornado vortex in the cyclostrophic balance region, r_c, and the pressure P is normalized by $1/2\rho V_c^2$. The radial profiles of the tangential mean velocity V of the numerical TLV simulated by the three sets of meshes are presented and compared in Fig. 3(a), where the velocity and radius are normalized by V_c and r_c. The numerical results agree well with the single-cell TLV generated in the experiment conducted by Cao *et al.* (2015), validating the numerical model and scheme in this study. Moreover, snapshots are taken by a sampling frequency of 100 Hz for a rectangular 3D region where $x, y \in [-0.1\text{m}, 0.1\text{ m}]$, and $z \in [0, 0.2\text{ m}]$, as illustrated in Fig. 1.

To accurately validate the LES results, the resolved spectrum indicated by the resolution for the turbulence kinetic energy (TKE) is calculated (Celik *et al.* 2005; Li *et al.*, 2022). The resolved TKE is defined as (Celik *et al.* 2005; Li *et al.*, 2022)

$$E \approx k_r/k_{all}, \tag{4a}$$

$$k_{all} = k_r + k_{sgs} + k_{num}, \tag{4b}$$

$$k_r = 0.5(\overline{u'^2} + \overline{v'^2} + \overline{w'^2}), \tag{4c}$$

$$k_{sgs} = \nu_{sgs}^2/L_s^2, \tag{4d}$$

where $\overline{u'^2}$, $\overline{v'^2}$, and $\overline{v'^2}$ are the variance of the fluctuating velocities u', v', and w', respectively. k_{num} represents a pseudo-energy term introduced by error during numerical calculation. The discretization in this study is second order, and the time step is also sufficiently small. Therefore, k_{num} becomes sufficiently small and can be neglected (Celik *et al.* 2005; Li *et al.*, 2022). Figure 3(b) presents the resolved spectra of the plane $z/h = 0.5$. Obviously, the grid in this study resolved at least 99% of the TKE.

Another index quantifying the resolution of a LES grid is the LES_{IQ}, which is defined as

$$LES_{IQ} = \left[1 + \alpha_\nu \left(\frac{\nu_{sgs} + \nu}{\nu}\right)\right]^{-a_e}, \tag{5}$$

where $\alpha_\nu = 0.05$ and $a_e = 0.53$. Celik *et al.* (2005) stated that $\text{LES}_{\text{IQ}} > 0.8$ indicates a proper LES and $\text{LES}_{\text{IQ}} > 0.9$ indicates a direct numerical simulation. Figure 3(c) shows the LES_{IQ} contours of the plane $z/h = 0.5$. The present grid achieved at least the LES resolution in all domains.

III. METHODOLOGY

A. Delayed proper orthogonal decomposition (d-POD)

The proper orthogonal decomposition (POD), one of the dimensional reduction and feature extraction statistical methods, has been extensively adopted in the study of mode identification and reconstruction from flow field (Chang *et al.*, 2021; De Cillis *et al.*, 2021; Moon and Manuel, 2021; and Zhu *et al.*, 2024a). POD minimizes the complexity of training data and lowers computation cost by converting high-order and non-linear wind pressure time series into low-dimensional signals. The flow field can be decomposed into two components using POD: the spatial-dependent coherence mode and temporal-dependent mode coefficients. Mathematical tools, including ARMAX and LSTM (Atam *et al.*, 2017), have been provided in previous studies to predict the flow field by fitting the temporal-dependent

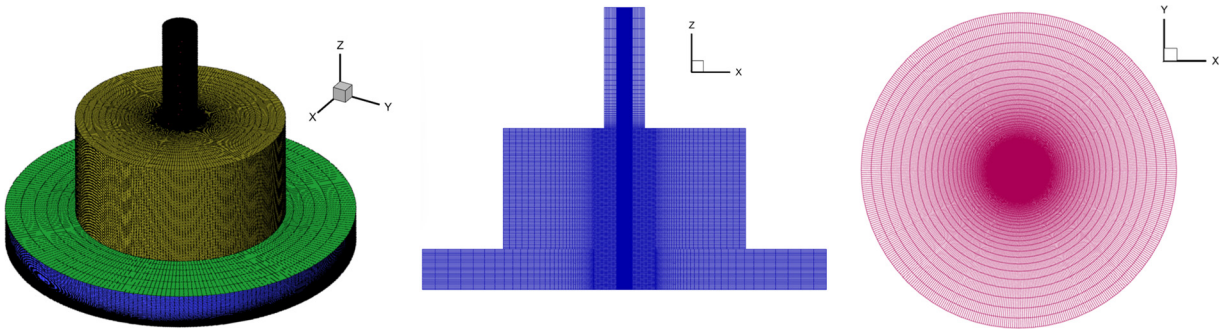

FIG. 2. Global and local mesh scheme of the numerical simulation (a) perspective view; (b) side view; (c) top view.

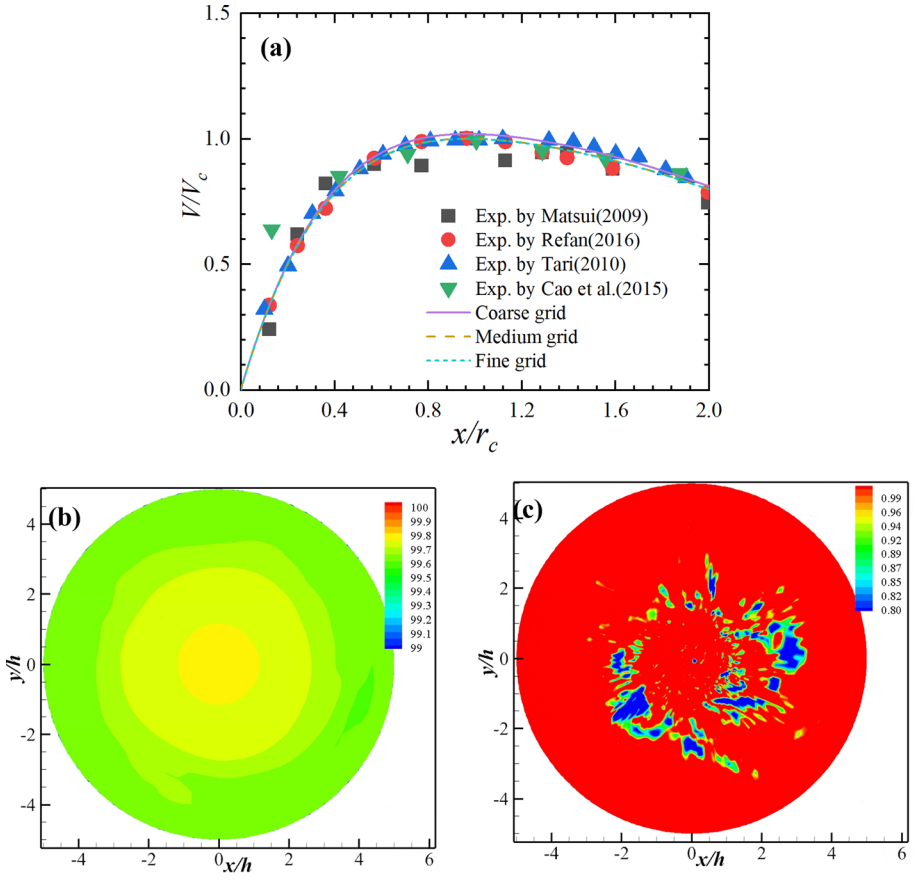

FIG. 3. (a) Comparison of radial profiles of the normalized mean tangential velocity in the previous study and present study. Contours of (b) time-averaged resolved spectra of the TKE and (c) LES_{IQ} index at the plane $z/h = 0.5$.

mode coefficients extracted from conventional POD. However, if the flow dynamics become chaotic, the mathematical tools mentioned earlier may not be accurate enough or may even fail, as the temporal mode coefficients become random to some extent, which is mathematically represented by a continuous spectrum (Li and Wu, 2020; Zhou *et al.*, 2023).

Notably, tornadoes differ from synoptic winds in that they exhibit strong variations in velocity, pressure, and temperature, resulting in the dynamical feature of tornadic flow field characterized with high-dimensionality, non-linearity, and complexity. Therefore, the mode coefficients extracted from the tornadic flow field show continuous spectrum rather than discrete spectrum, which makes the mode's temporal prediction arduous. Fortunately, the delayed embedding theorem can reconstruct the dynamics through time-delayed embedding for complex dynamic system, that is because delay embedding can lift a time series signal into a higher dimensional space by stacking it with time-shifted copies of itself. This method, rooted in the foundational Takens embedding theorem, allows for the reconstruction of a chaotic attractor—up to a diffeomorphism—from the time series of a limited number of measured variables. Previous studies have found that time-delayed POD exhibits similarities to Fourier or wavelet bases (Dylewsky *et al.*, 2022). Specifically, it has been shown that with sufficiently long embedding windows, the delay coordinate POD converges to an estimate of the discrete Fourier decomposition (Dylewsky *et al.*, 2022). In essence, as the embedding windows increase (i.e., the delayed embedding number d in this study), the time series become smoother and gradually resemble harmonic curves (Das and Giannakis, 2019). It is well-known that time series from chaotic dynamic systems exhibit some degree of randomness. Mathematically, these time series present a continuous spectrum in the frequency domain. The d-POD can enhance the discrete system eigenvalues by embedding additional shifted copies of the data, thereby increasing the dimension of the augmented space (Das and Giannakis, 2019). This data operation allows a sufficiently dense point spectrum to approximate a continuous one. Consequently, d-POD is superior to POD when dealing with chaotic time series. Moreover, it also performs well in mode extraction and prediction in special situations, such as strongly nonlinear systems under noise interference and complex dynamic system with mismatched space-time dimensions (Dylewsky *et al.*, 2022).

To obtain better tornado flow field prediction results, d-POD, which introduces the Taken's embedding theory into POD, is employed to extract the time-dependent mode coefficient of the 3D mode. The detailed algorithm of d-POD can be found in the Appendix. It has been also described in our previous work in (Zhou *et al.*, 2023).

B. Multi-functional recurrent fuzzy neural network (MFRFNN)

MFRFNN (multi-functional recurrent fuzzy neural network) is a neural network model that that is used in various applications such as

pattern recognition, prediction, and control (Nasiri and Ebadzadeh, 2022). MFRFNN consists of two recursive fuzzy neural networks with Takagi-Sugeno-Kang (TSK) fuzzy rules: one for generating the output network and the other for determining the state of the system (called the state network). The output network uses K_1 fuzzy rules to perform N function approximations on N states of the system, that is, each state learns a function, and the system output is composed of the sum of these functions. The state network also uses K_2 fuzzy rules to perform N function approximations to determine the next state of the system. The two networks are connected through a feedback loop, which enables MFRFNN to remember the historical information of past observations and learn multiple functions simultaneously, thereby capturing the dynamic characteristics of chaotic time series. More details of the state network, training algorithm, and prediction algorithm can be found in Nasiri and Ebadzadeh, 2022.

Figure 4 demonstrates the structure of MFRFNN. As shown in Fig. 4, both networks consist of five layers, that is, input layer, fuzzy rule layer, normalized fuzzy rules layer, extended fuzzy rules layer, and output layer. In the training phase, MFRFNN selects parameters through trial and error, such as the number of fuzzy rules of the output network and state network, the number of states of the state network, and the maximum number of fitness evaluations of the particle swarm optimization algorithm. Here, the layer number is selected as 5. Layer 1 is the input layer, which receives input variables, and its neurons correspond to membership functions (MFs). $a = [a_1, a_2, \ldots, a_n]^T$ and $\hat{y}$ represent the input and predicted output, respectively. $A_{i,j}$ and $B_{i,j}$ denote the MFs for a_i in the ith rule of output and state network, respectively. Layer 2 represents the fuzzy rules, and their output represents the firing strength of a rule. The outputs r_i and q_i of the ith neuron in the output and state networks are calculated using Eqs. (6) and (7), respectively,

$$r_i(\mathbf{a}) = \prod_{j=1}^{d} \mu_{A_{i,j}}(a_j), \tag{6}$$

$$q_i(\mathbf{a}) = \prod_{j=1}^{d} \mu_{B_{i,j}}(a_j), \tag{7}$$

where $\mu_{A_{i,j}}(a_j)$ and $\mu_{B_{i,j}}(a_j)$ denote the membership values of jth input variable x_j. Layer 3 is the output of the neurons in this layer that represents the normalized firing strength of each rule, which is calculated as follows:

$$\bar{r}_i(\mathbf{a}) = \frac{r_i(\mathbf{a})}{\sum_{j=1}^{K_1} r_j(\mathbf{a})}, \tag{8}$$

$$\bar{q}_i(\mathbf{a}) = \frac{q_i(\mathbf{a})}{\sum_{j=1}^{K_2} q_j(\mathbf{a})}. \tag{9}$$

Layer 4 is N linear combinations of normalized firing strength of rules are computed in this layer. F_i and G_i denote the output of approximated functions for the output and state networks, respectively, which can be computed as follows:

$$F_i = \sum_{i=1}^{K_1} \bar{r}_i w_{ij}, \tag{10}$$

$$G_i = \sum_{i=1}^{K_2} \bar{q}_i v_{ij}, \tag{11}$$

where w_{ij} and v_{ij} represent the link weight corresponding to the ith rule of the output and state network in the jth state of the system,

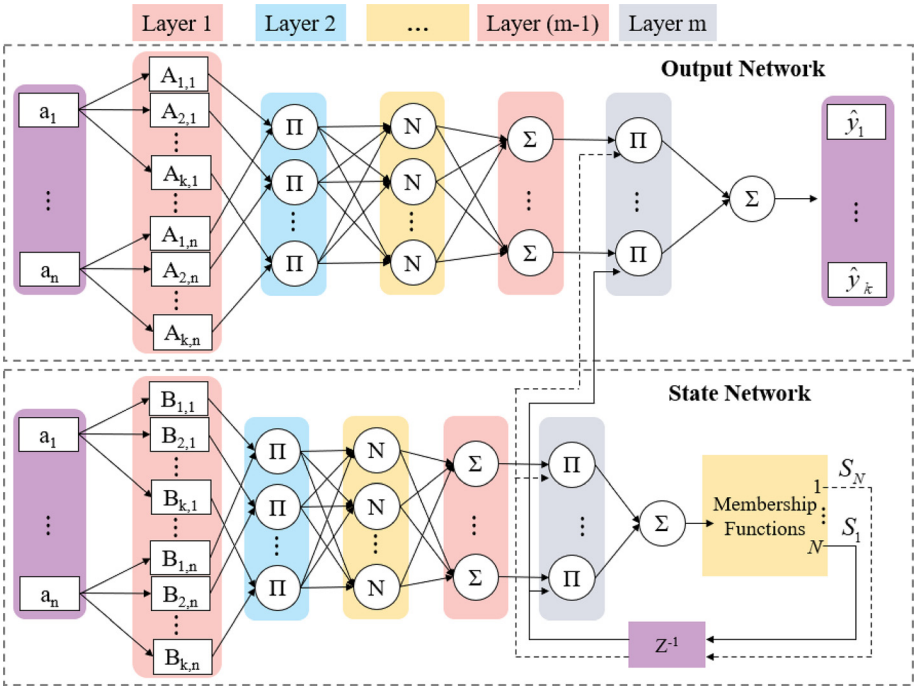

FIG. 4. Schematic of MFRFNN architecture. The output network generates the system's output, and the state network is responsible for producing state signals.

respectively. Layer 5 is the output layer. The output of the system at the time step t, $(\hat{y})$ is computed as follows:

$$\hat{y}(t) = \mathbf{F}(t)^T \mathbf{S}(t), \tag{12}$$

where $\mathbf{F}(t)$ and $\mathbf{S}(t)$ denote vectors whose entries are the output of approximated functions and state signals of the system at the time step t, respectively, as presented in the following equations:

$$\mathbf{F}(t) = [F_1, F_2, \ldots, F_N]^T, \tag{13}$$

$$\mathbf{S}(t) = [s_1, s_2, \ldots, s_N]^T. \tag{14}$$

To sum up, as an innovative time series prediction model, MFRFNN can learn multiple functions at the same time and handle the dynamic changing characteristics of the time series by combining the output network with the state network and the feedback mechanism. Therefore, in this paper, MFRFNN is used to predict the modal coefficient time series extracted by d-POD.

C. 3D mode-based recurrent fuzzy framework

The aim in this study is to enhance the prediction efficiency and accuracy of the time series of physical quantities in flow fields by combining d-POD with the MFRFNN model. Figure 5 demonstrates the process to achieve this goal. Specifically, the proposed framework involves the reduction of the high-dimensional tornadic flow field's dimensionality using d-POD. With the aid of d-POD, the flow field can be decomposed into spatial-dependent coherence modes and temporal-dependent mode coefficients, and smoother mode coefficients representing enhanced intrinsic feature can be identified by d-POD. Subsequently, a novel multi-functional recurrent fuzzy neural network, MFRFNN, is utilized to forecast the time-history of mode coefficients. Eventually, the prediction of wake is accomplished by reconstructing the flow field using the predicted mode coefficients and their corresponding modes.

IV. RESULTS AND DISCUSSION

A. Mean, fluctuating, and statistical flow feature of the tornado-like vortex

Figure 6 shows the time-averaged flow field contour of normalized representative physical quantities of the single-cell TLV. When the airflow converges toward the center of the tornado, the radial velocity U is defined as negative and vice versa. As can be seen in Fig. 6(a), above the height of $z/h = 0.4$, U is almost zero within the region from $x = -r_c$ to $x = r_c$, which indicates the radial convection effect has vanished. Notably, a strong radial jet flow is generated close to the ground ($z/h < 0.05$) whose maximum radial velocity reaches $-V_c$ outside of the vortex core region (as indicated by red arrow). When this radial jet flow reaches the core vortex region, based on the momentum conservation law, this lower jet flow must change its direction from the radial to the vertical direction, and thus, upper jet flow with positive direction is generated and concentrated within the inclined region. There are also strong vertical velocities adjacent to the oblique region occupied by this upper jet flow, as shown in Fig. 6(c). The intense tangential velocity appears in the lower part of the TLV, forming a strong annular vortex, which is sandwiched between the two inward and outward jet flows, as shown in Fig. 6(b) Negative pressure appears in the vortex core area; moreover, its distribution remains basically unchanged along the height but slightly shrinks and narrows

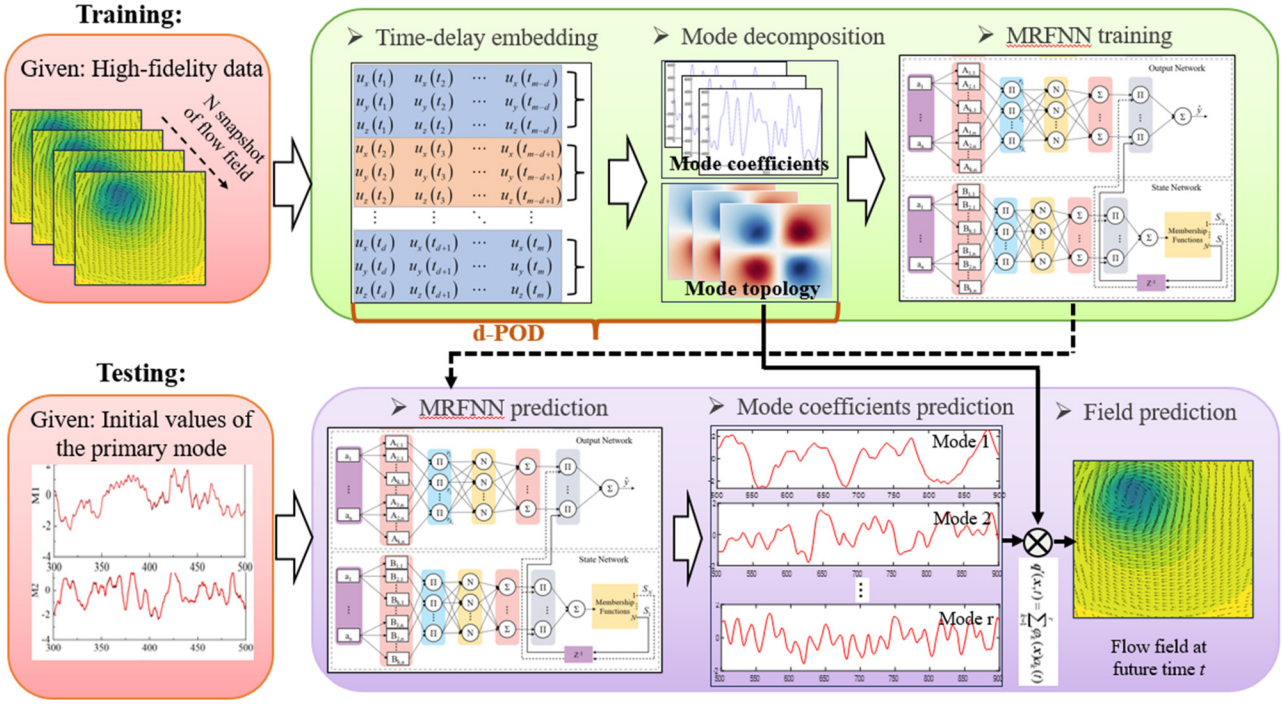

FIG. 5. 3D mode-based recurrent fuzzy framework for flow field prediction.

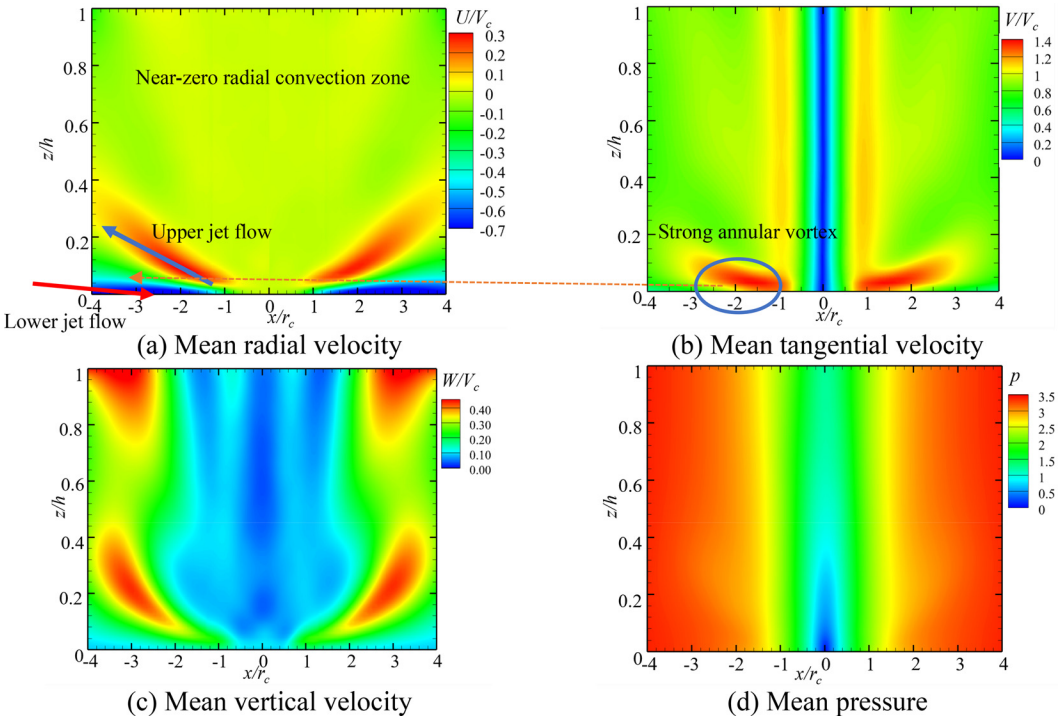

FIG. 6. Time-averaged flow field contour of normalized representative physical quantities of the single-cell TLV.

near the ground, as depicted in Fig. 6(d). It is also found that the vertical velocity begins to be not enough to resist the reverse pressure gradient, which possibly lead to the backflow of TLV within the vortex core. This phenomenon demonstrates that TLV in this case is the still single-cell vortex structure but in the transition stage where the vortex is about to break.

Figure 7 shows fluctuating flow of normalized representative physical quantities of the near-break-down TLV. The fluctuating radial velocity shows a peak root mean square (RMS) value of $0.6V_c$ at the height of $z = 0.08h$ near the ground. This fluctuation in the radial direction is concentrated in the center of the vortex structure, especially at the bottom, which manifests that the wandering effect of the vortex core is notable. It is evident that the relatively large fluctuating tangential velocity appears at the similar location where its average value reaches the maximum. This is induced by the effect of the bottom annular vortex and can be further confirmed by the instantaneous vortex structure described below. The high-speed annular vortex at the bottom is provided with relatively intensive stability, so its protective effect causes the vortex breakdown lag occurring at the bottom part compared to the upper part. In addition, the intensive fluctuating vertical velocity also emerges at the location of upper jet low. Turbulent kinetic energy is the sum of three mutually perpendicular fluctuating velocity components. Interesting, its distribution is roughly consistent with the fluctuating tangential velocity distribution, which indicates that the fluctuation of the entire TLV-induced wind field is mainly dominated by tangential velocity fluctuation.

Figure 8 qualitatively examines the vertical distribution of the mean and fluctuating velocity components at different radial distances. During the near vortex breakdown stage, because of ground interference, the variation of both mean and fluctuating velocity components in radial, tangential, and vertical direction all present drastic trend near the ground but become basically unchanged in the upper part. At the vortex core center ($r = 0$), the mean value of the three velocity components slightly fluctuates around 0. As the radial distance increases, the velocity variation trend along the vertical height is more dramatical, especially for the axial velocity component. The fluctuating velocity is more sensitive to radial distance. In general, the largest fluctuating radial and vertical velocity both appear at the center of the vortex core, while the strongest fluctuating tangential velocity emerges at the radius of the vortex core. In addition, the mean and fluctuating tangential velocity is significantly larger than its counterparts of the radial velocity and vertical velocity, manifesting tangential velocity is the primary characteristic of tornadoes.

To present three-dimensional structure of the tornado-like vortex, Fig. 9 shows the 3D streamlines in the whole tornado simulator and 2D streamlines superimposed on instantaneous vertical vorticity contour maps on three horizontal planes in the converge chamber. Figure 9(a) gives an overview of the fluid flow inside the simulator. It shows that tornado-like vortices (rotating and going up) are generated in the three regions including the convergence, convection and exhaust chamber. As can be seen in Fig. 9(b), the core size variation with height is almost negligible. The maximum vorticity is observed at the center of the vortex and the vorticity decreases roughly from the inside out. Notably, although the flow shows axisymmetric characteristics, the vortex cores on three horizontal planes do not coincide with the geometric center of the computational domain, suggesting the occurrence of the vortex core wandering phenomenon.

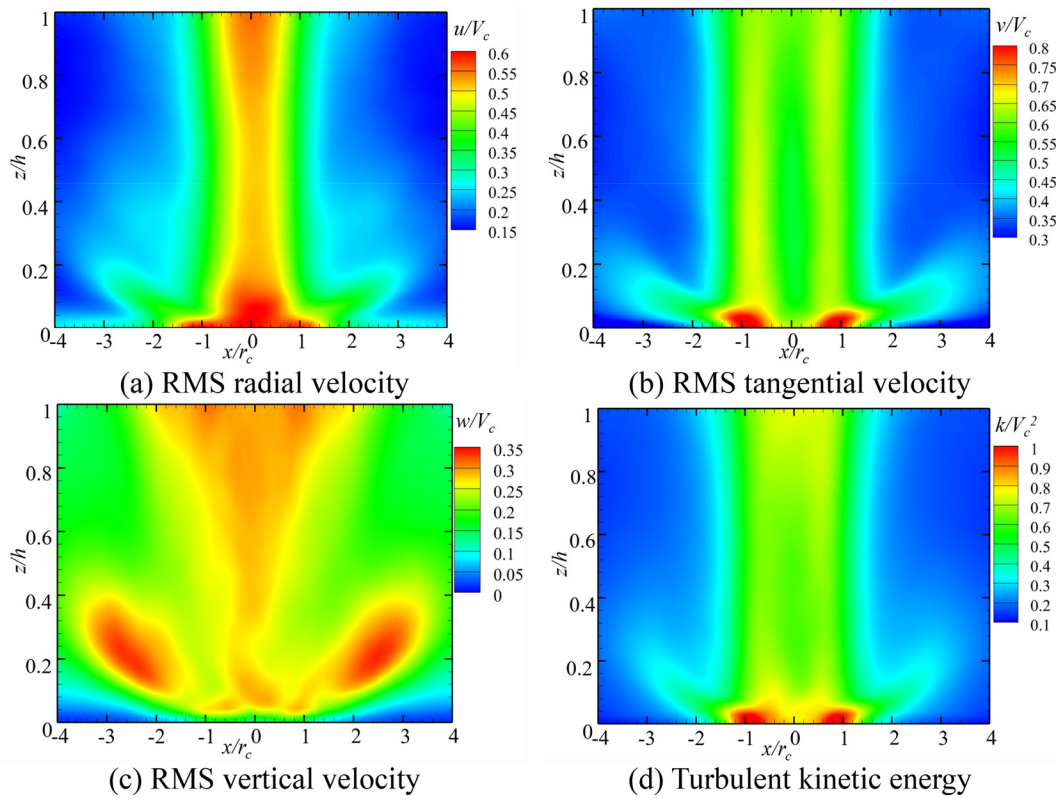

FIG. 7. Fluctuating flow field contour of normalized representative physical quantities of the single-cell TLV.

B. 3D coherent structure identification and interpretation

In this section, to reveal the dominant turbulent flow characteristics in TLV and the potential relationship between its dynamics and the coherent structures, the spatial 3D mode morphology and the temporal evolution of mode coefficients are identified and interpreted. Here, fully developed flow field data were collected. Here, the time interval between each snapshot was $\Delta T = 20\Delta t$. Figure 10 shows the energy proportion of each mode (denoted by the black box) and the accumulative energy percentages of the first 40th modes (represented by the red dot). The primary modes are selected and ranked from the highest to the lowest based on turbulent energy. The three-dimensional coherent structure of the first and third predominant modes is depicted in Fig. 11. The coherence mode is presented using the iso-surface of vertical vorticity. Red represents the positive direction of rotation, and blue represents the negative direction.

It can be observed in Fig. 10 that the energy occupation of the first and second modes is roughly similar, which is approximately 43%. Interestingly, it should be noticeable that even though relative positions in space are different, the spatial shapes of mode 1 and mode 2 (not present here) are with evident similarity. This observation can be well confirmed by the statement in Taira *et al.* (2017) that with real-valued POD modes, it is a pair of stationary modes, which is similar in shape but appear shifted in the advection direction that can represent the traveling structure instead of a single mode.

The distribution of the coherent vortex structure exists distinctive differences in the vertical direction, indicating that the three-dimensional characteristics of the tornado vortex structure are significant and necessary to be taken into consideration. In addition, the centers of the coherent mode and the geometric center are not overlapped, indicating that the first two main modes are dominated by the wandering effect of the tornado vortex. This result is like the 2D POD modal results decomposed from the TLV flow field obtained by PIV test in Karami *et al.* (2019).

The first 40 modes account for more than 90% of the turbulence energy, while the sum of the energy proportion of the first three modes is close to 60%, which shows that the first three modes play a dominant role in the dynamic characteristics of the 3D vortex structure of the tornado. As shown in Fig. 11(b), the third-order mode shape is a single vortex structure, which exists independence without conjugate vortex pairs. It is obviously different from the first two modes and possibly induced by the strong nonlinearity of the TLV dynamical system.

C. 3D tornado-induced flow field prediction

In this section, the 3D mode-based surrogate model is evaluated in their capacity to predict the future state of the unsteady tornadic flow field. Figure 12 compares the temporal evolution of the first three mode coefficients between the real result and the predicted result. The first three modal coefficients have been regularized by dividing their

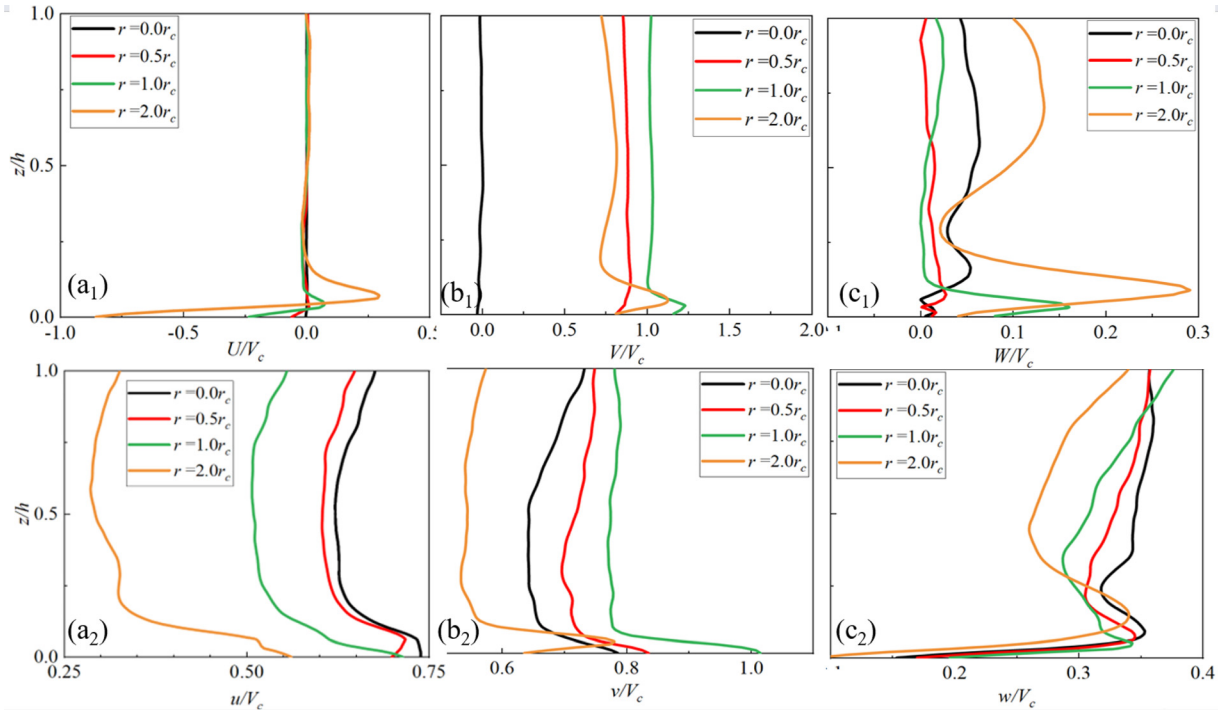

FIG. 8. Vertical distribution of time-averaged velocity and fluctuating velocity at different radial distance for (a) radial component; (b) tangential component; (c) vertical component.

respective root mean square values, i.e., $C_{Mi}(t) = Mi(t)/\sigma_{Mi}$ ($i = 1, 2, 3$), and time has also been dimensionless by $t* = t*V_c/2r_c$. The fluctuation of the modal coefficients mainly reflects the dynamic characteristics of the vortex wandering. As shown in the figure, the first three modal coefficients of the tornado mode have no obvious regularity, which means that the vortex wandering has a certain degree of randomness. For time series prediction, we select the mode coefficients at time $t^* = 0$–300 as the training set to train the prediction model. During the testing process, only the first 20 time steps of ground truth data (i.e., real mode coefficient) are employed to predict the next time step, after which only the predicted fields are used to evolve the flow till the end of the time series.

The root mean square value (RMS) is calculated over the testing regime using the following equation:

$$Error = \sqrt{\frac{1}{N}\sum_{i=1}^{N}\left(u_{real,i} - u_{predict,i}\right)^2 / u_{real,i}^2}, \tag{15}$$

where N represents prediction for the next Nth time step, herein, $N = 1$.

As shown in Fig. 12, the 3D mode-based-FNN method can accurately predict the temporal evolution and power spectral density (PSD) of modal coefficients in time extracted from the tornadic flow field, and the RMSE errors are all less than 0.8%.

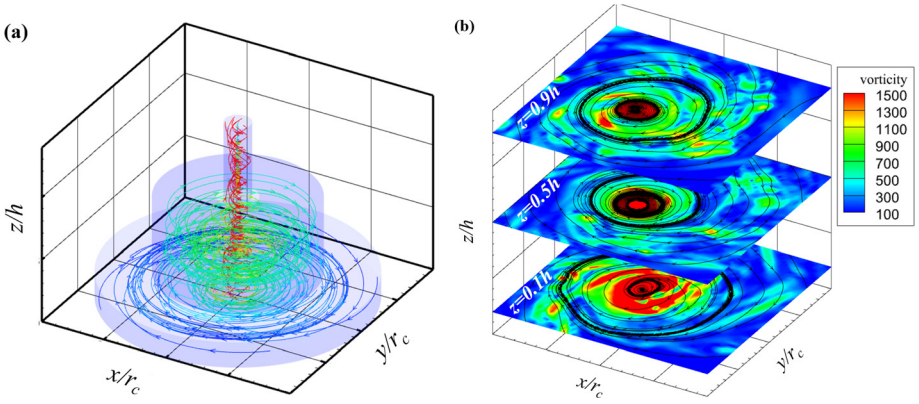

FIG. 9. (a) 3D streamlines in the whole tornado simulator; (b) instantaneous streamlines colored by instantaneous vorticity on horizontal planes at $z/h = 0.1$, $z/h = 0.5$, and $z/h = 0.9$. Velocity denotes the resultant of the radial, tangential vertical velocity components.

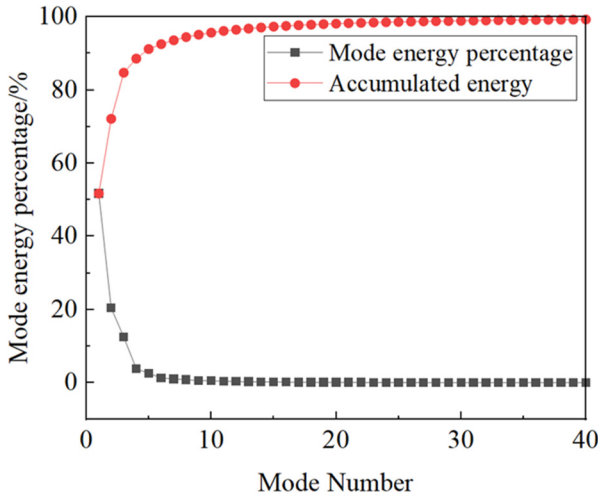

FIG. 10. Energy percentage taken by the primary modes and their accumulated energy proportion.

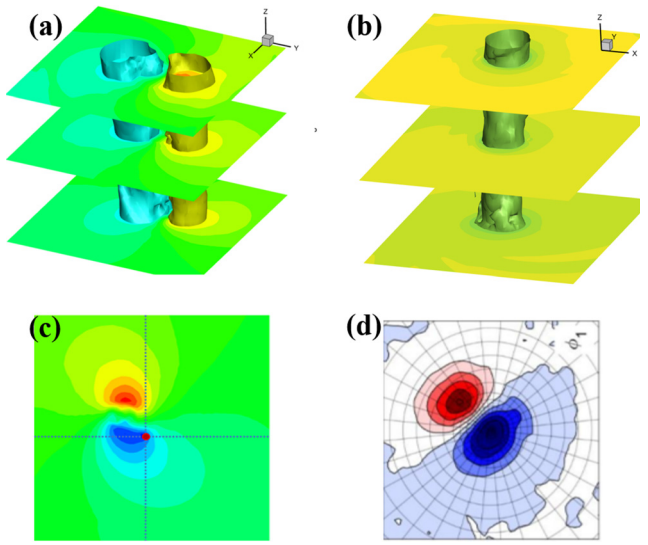

FIG. 11. The three-dimensional vorticity POD modes of (a) the first mode and (b) the third mode, positive (negative) values of vorticity are shown in red (blue). The comparison of the first POD mode in 2D slice plane of (c) current study and (d) Karami *et al.* (2019).

Figures 13 and 14 compare the velocity vector plot superimposed pressure contour between the real result and the predicted result at time $t^* = 450$ at the target region on three different horizontal planes ($z = 0.02$, 0.1, 0.2) and the vertical plane ($y = 0$), respectively. The predicted value is obtained by taking the first fifth modes as the input value, while the real value is the reconstruction of the first fifth modes (the same method is used for the real values mentioned later), the relative error between the predicted value and the real value is also given and defined as $Error = |u_{real} - u_{predict}|/|u_{real}|$. As can be observed on Fig. 13, the center of the vortex core on the three horizontal planes from the lowest to the highest is located on $(x,y) = (0.021, -0.023)$, $(0.015, -0.005)$, and $(0.018, 0)$, respectively, which is evidently deviate

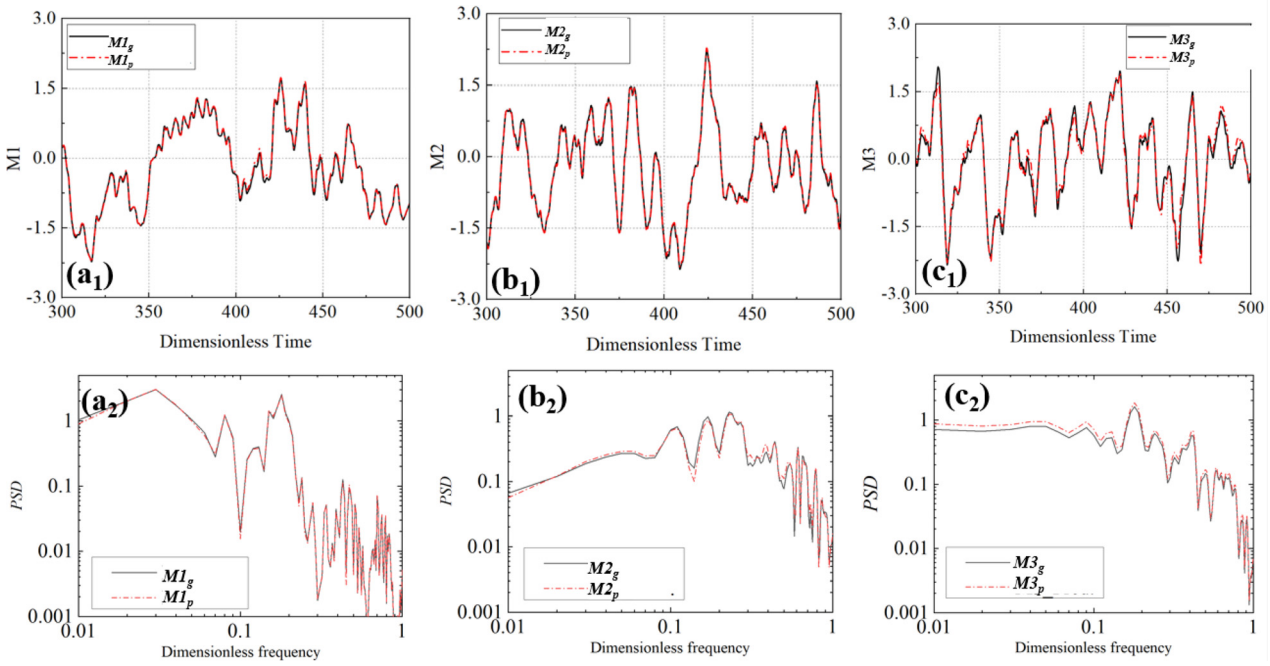

FIG. 12. Comparison of the temporal evolution (a_1)–(c_1) and PSD (a_2)–(c_2) of the first 3D mode coefficients between the real result and the predicted result. Note that the subscript "g" means ground true, and "p" means prediction.

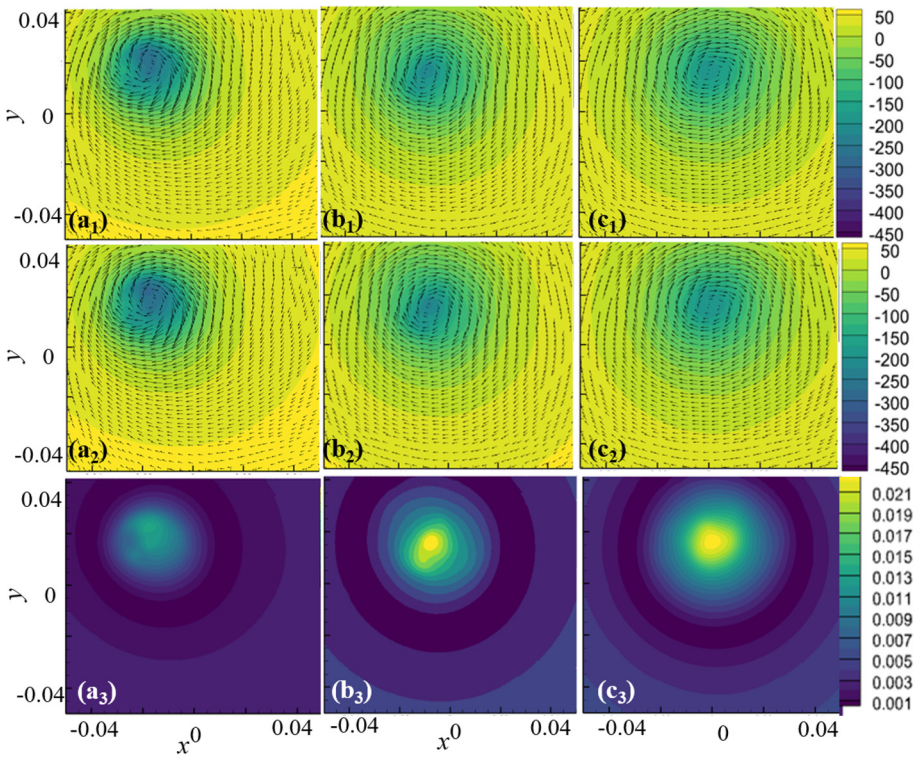

FIG. 13. Comparison of the velocity vector colored by pressure contour on three horizontal planes $z = 0.02$, 0.1, and 0.2 (from left to right) at the normalized moment $t^* = 450$ between the real result and the predicted result (a_1)–(c_1), (a_2)–(c_2) and their relative error (a_3)–(c_3).

from the geometry center. It can also be observed that the extreme value of the negative pressure appears at the vortex core, whose value is strengthened with the increase in the height of horizonal plane. This phenomenon manifests that the 3D TLV structure is distorted in the vertical direction, and Fig. 14 further demonstrates this observation that the vortex intensity in the lower part of the TLV is greater than the that in the upper part, which is possibly because of the generation of shear instability that causes the vortex core to meander. It can be concluded from Figs. 13 and 14 that the prediction method proposed in this paper can accurately predict the instantaneous 2D-plane tornadic flow field. The spatial shape of the predicted flow field is basically consistent with the real flow field. The maximum prediction error is located at the vortex core, and the maximum errors are less than 2%.

To further verify the correctness of the prediction results, the radial and vertical distributions of the true and predicted mean velocity components at the target field of the TLV are quantitatively compared in Figs. 15 and 16. Here, the subscript "g" means ground true, and "p" means prediction. It can be seen that the predicted velocity profile generally agrees well with the simulated real data at three different heights and on the vortex core center, which validates the effectiveness of the proposed surrogate prediction model in this study. Although there exist relatively obvious differences in the extreme value, the largest

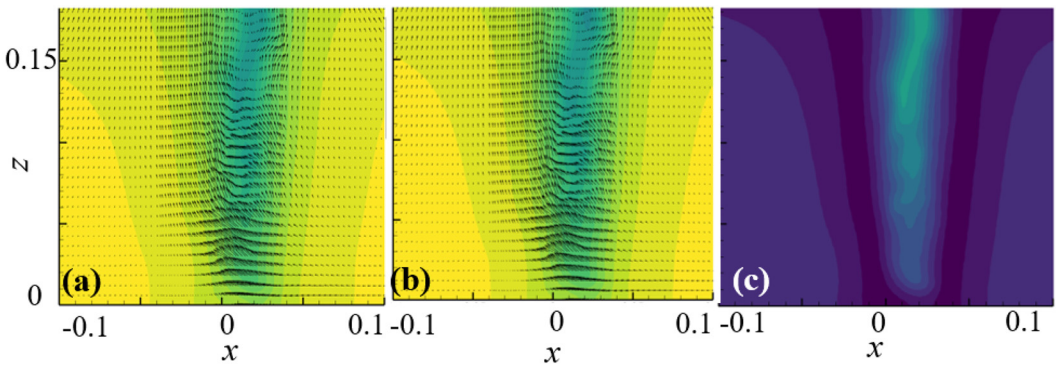

FIG. 14. Comparison of the velocity vector colored by pressure contour on the vertical planes $y = 0$ at the normalized moment $t^* = 450$ between the real result and the predicted result (a), (b) and their relative error (c).

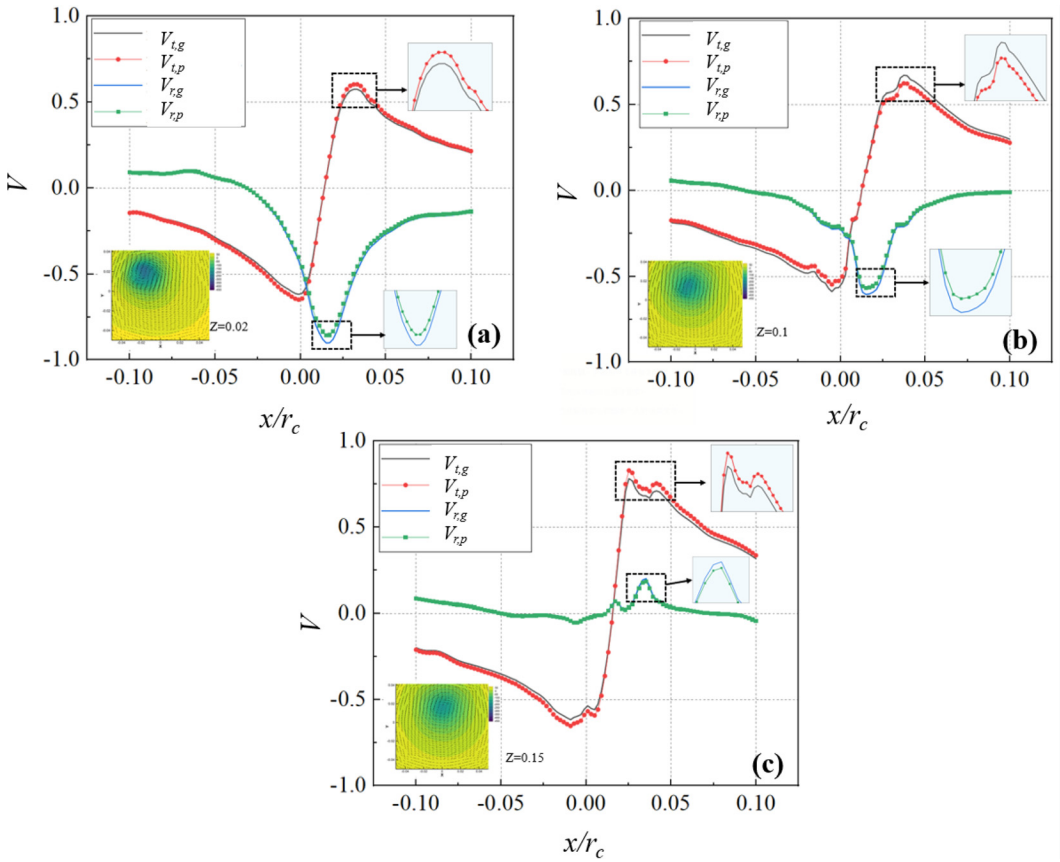

FIG. 15. Comparison of the radial distribution of the radial velocity and tangential velocity component at three horizontal planes $z =$ (a) 0.02, (b) 0.1, and (c) 0.15 between the real result and the predict result. Note that the subscript "g" means ground true, "p" means prediction, "t" means tangential velocity, and "r" means radial velocity.

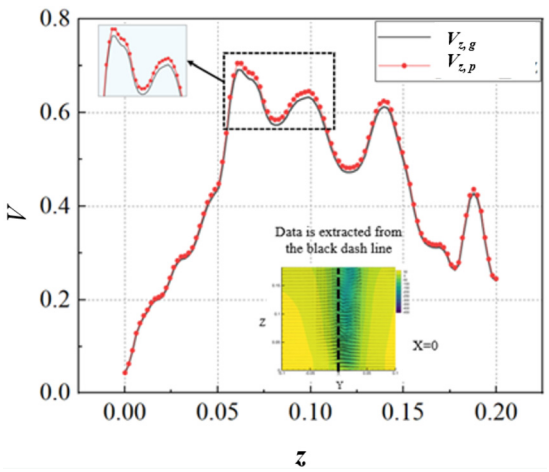

FIG. 16. Comparison of the vertical distribution of the vertical velocity component at the horizontal plane $y = 0$ between the real result and the predict result.

deviation error between the predicted velocity from the real value is no more than 2%.

In addition to assessing the quantitative distribution of one-dimensional velocity components profile and qualitative distribution of the two-dimensional plane velocity contour, the three-dimensional vortex structure represented by the vorticity is also presented and compared between the predicted values and the real value as shown in Fig. 17. It is evident that despite the discrepancy exists in detail and local, especially in the small area near the ground ($z < 1$ mm), where the velocity gradient is large, the global spatial shape and dynamic feature of the tornado-like vortex structure are with acceptable similarity, presenting the essence of the swirling jet flow (i.e., the recirculation bubble and the sense of rotation of the swirling jet).

D. Parametric analysis

1. Number of fuzzy rule and time-delayed number

The structure parameters of the fuzzy neural network and the mode extraction method can be main factors affecting the prediction

FIG. 17. Comparison of the instantaneous vortex structures ($Q = 1.8 \times 10^5$ s^{-2}) colored by pressure between the (a) real result and (b) predict result.

accuracy of 3D TLV flow field. Thus, this section aims to study the impact of three key parameter contained in the aforementioned main factors, specifically, for the fuzzy neural network structure, the influence of the number of fuzzy rules of the output network and state network (*K1* and *K2*) on the result is investigated; while for the mode identifying method employed in this study, the influence of the time-delayed number (*d*) is also discussed. Figure 18 presents the variation of the root mean square value of the predicted value and the real value with three key parameters for the first three-order mode coefficients and the first total 20% mode coefficients extracted from TLV flow field. Note root mean square value is calculated in Eq. (14), and the number of forward prediction step *N* is 1. Figure 18(a) shows the variation of RMS value with the delayed-time number. It is reported that both delayed in time and embedding in spatial are effective measure to expand the dimensionality of the dynamic system that helps to efficiently reveal its essence. In theory, as the increases of delayed-time number, time series decomposed by d-POD become smoother that facilitates more accurate prediction results. However, when *d* is too large, there may be a mismatch between the temporal and spatial dimensions, which may lead to a deterioration in the prediction accuracy of modal coefficients. This speculation has also been confirmed in Fig. 18(a), that is, it can be observed that the root mean square error decreases first and then increases with the rise of *d*, and the optimal RMS error result appears around $d = 8$, and the errors of the four types of mode coefficients investigated here are not greater than 1%. However, when *d* is greater than 16, the root mean square error significantly increases. Overall, the RMS errors of the prediction result for mode 1 (M1) and mode 2 (M2) are smaller than that of mode 3 (M3), indicating that the lower the modal order, the more accurate the prediction is. For parameters *K1* and *K2*, as shown in Figs. 19(b) and 19(c), it can be seen that the prediction error of M1 and M2 is smaller than M3, indicating the prediction accuracy for the predominant mode achieves better performance compared to others possibly because the temporal evolution of the lower-order mode is smoother and more regulative. In addition, as *K1* and *K2* increase, the root mean square error generally shows a decreasing trend, but when *K1* and *K2* are greater than 18, the error no longer decreases. Moreover, the RMS error for all the four cases is not greater than 0.2%. Therefore, in this study, when predicting the flow field time series of tornado-like vortex, *d* is taken as 8, and *K1* and *K2* are taken as 18.

2. Number of forward steps for future prediction

Figure 19 shows the root mean square error between the predicted and true values for different physical quantities at two different number of forward steps for future prediction. The error is calculated by the following equation:

$$Error = \sqrt{\frac{1}{M}\sum_{i=1}^{M}\left(\frac{1}{N}\sum_{j=1}^{N}\left(u_{real,i,j} - u_{predict,i,j}\right)^2 \Big/ K u_{real,i,j}^2\right)}, \quad (16)$$

where *M* is the number of spatial points in the target region, *K* is the number of forward predictions each time, and *N* is the number of predicted time series. When $K = 1$, as shown in Fig. 19(a), there is not much difference in prediction error between different physical quantities. This method is more accurate in predicting *Vz*, with an error of less than 0.03%. The maximum prediction error for pressure field *P* is

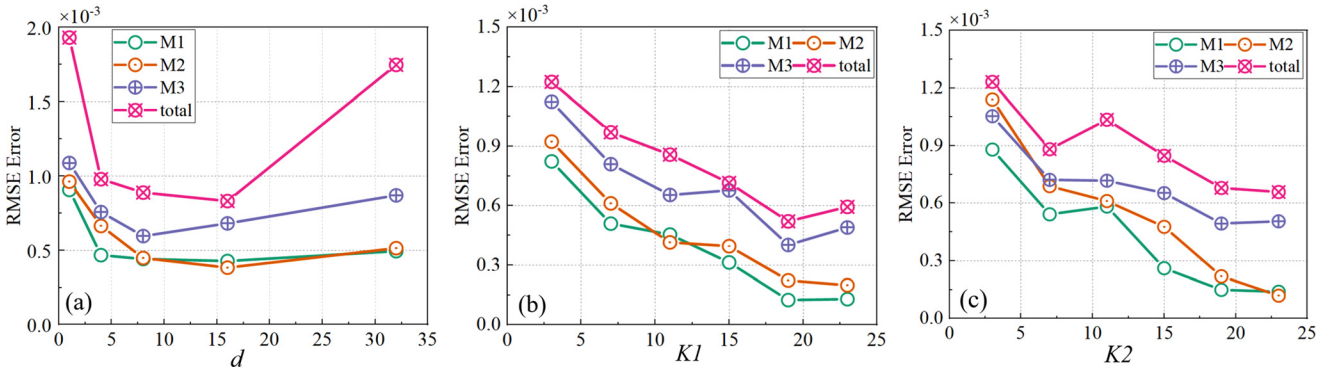

FIG. 18. Variation of RMS value of the predicted error with the key parameter in the 3D mode-based Recurrent Fuzzy Framework: (a) time-delayed number *d*; (b) *K1*; (c) *K2*.

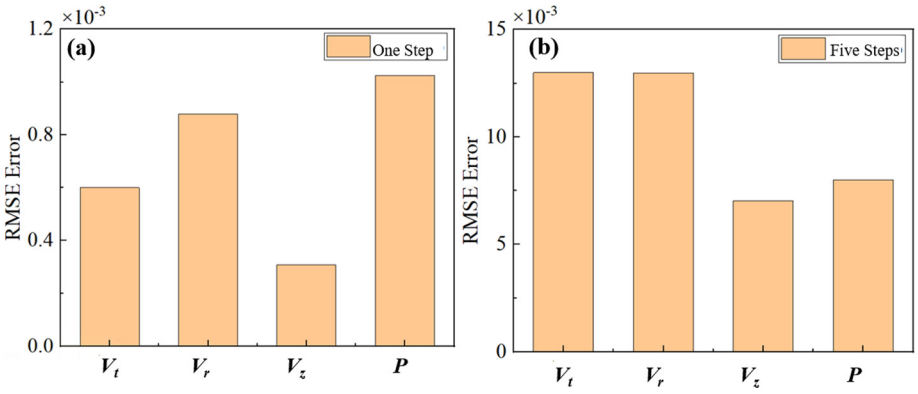

FIG. 19. RMS value of the predicted error at the future first step (a) and at the future fifth step (b).

not greater than 0.1%. When K increases to 5, the overall error is greater than the prediction effect when $K = 1$. As shown in Fig. 19(b), the prediction error of Vz is the smallest and less than 0.7%, while the prediction error of tangential velocity Vt is the largest but not more than 1.1%.

The comparison of two operating conditions indicates that the accuracy of prediction is more sensitive to parameter K. To further investigate the impact of parameter K on prediction accuracy, the overall error varies with parameter K as shown in Fig. 20, where the overall error is represented as the mean root mean square error of four physical fields. Overall, as K increases, the prediction error is also amplified. When K is less than 7, the prediction error slowly increases, and when $K > 7$, the overall root mean square error increases sharply. Therefore, it is recommended that when making multi-step predictions, the number of steps K should not exceed 7.

V. CONCLUDING REMARKS

In this paper, the near-break-down TLV is simulated in the ward-type simulator by large-eddy simulation. The three-dimensional coherent structure and its dynamics contained in TLV are identified and interpreted by the delayed-POD method. A novel 3D mode-based recurrent fuzzy framework is proposed to test in its capability to predict the spatiotemporal variations of mean velocity and pressure, flow statistics such as RMS value of the tornadic flow field. Parametric analysis is conducted to discuss the influence of the structure of the surrogate model and the number of time-delayed embedding on the prediction accuracy. The conclusion can be obtained as follows:

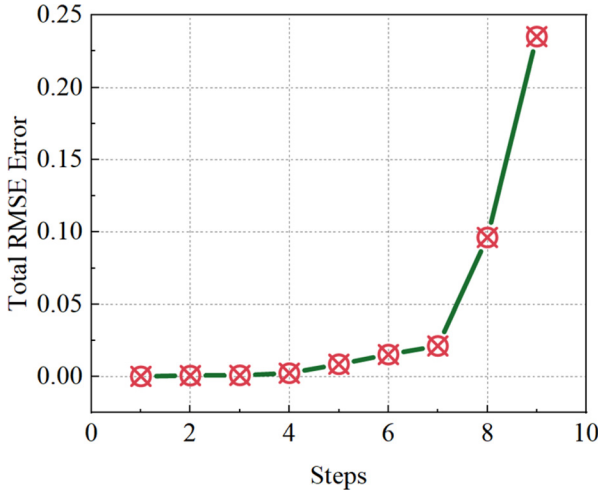

FIG. 20. Variation of RMS value of the predicted error with the future predicted step number.

In terms of the flow field of near-break-down TLV, it is found that inward and outward jet flows appear at the location close to the ground for the mean radial velocity, between these two jet flows, strong annular vortex is formed due to the intense tangential velocity, and its strong stability protects the vortex from breakdown up at the latest in the lower part. Moreover, vertical velocity becomes not drastic enough to resist the reverse pressure gradient, which potentially results in the backflow of the vortex core soon. The vortex wandering effect has a significant influence on the fluctuating characteristics of the near-break-down TLV.

The three-dimensional characteristics of tornado vortex structure are evident, exhibiting its features as the recirculation bubble and the sense of rotation of the spinning jet. Due to the strong momentum exchange in the vertical direction for the TLV, the variation of velocity and pressure with height are very intense, especially for the near ground location owing to the vertical shear effects. Thus, it can be inferred that it is difficult to accurately reproduce the three-dimensional dynamic characteristics of tornadoes with limited two-dimensional plane flow field.

The first 40 modes account for more than 90% of the turbulence energy, while the sum of the energy proportion of the first three modes is close to 60%. The first two modes are conjugate modes, which have similarity in the mode morphology, but are different relative positions in space, namely, their centers are significantly deviated from the geometric center, indicating that the first two main modes are dominated by the wandering effect of the tornado vortex. The third-order mode shape is a single vortex structure that is possibly induced by the strong nonlinearity of the TLV dynamical system.

The proposed 3D mode-based surrogate model can correctly predict the tornado-like vortex with a relative error of less than 2%. Three key parameters, including the fuzzy rules and time-delayed embedding number, in the fuzzy neural network and the mode extraction methods, have a significant effect on the prediction result. In this case, when predicting the flow field time series of tornado-

like vortex, d is taken as 8, and $K1$ and $K2$ are taken as 18. Increasing the number of forward steps for future prediction K could amplify the prediction error. Within the acceptable prediction accuracy, it is recommended that when making multi-step predictions, the largest K should not exceed 7.

This study is expected to enhance the understanding of three-dimensional coherent structure, and its dynamics contained in TLV, which provides an important theoretical basis for revealing the mechanism of interaction between tornadoes and structures. The prediction model proposed in this study with short-term forecasting ability is anticipated to offer reference for the warning and prevention of tornado-related disasters.

ACKNOWLEDGMENTS

This work was supported by the National Natural Science Foundation of China (Grant No. 12172109), by the Guangdong Basic and Applied Basic Research Foundation under Grant No. 2022A1515011492, and by the Shenzhen Science and Technology Program under Grant No. JCYJ20220531095605012.

AUTHOR DECLARATIONS

Conflict of Interest

The authors have no conflicts to disclose.

Author Contributions

Lei Zhou: Conceptualization (equal); Data curation (equal); Formal analysis (equal); Writing – original draft (equal). **Bernd R. Noack:** Supervision (equal). **K. T. Tse:** Supervision (equal). **Xuhui He:** Supervision (equal).

DATA AVAILABILITY

The data that support the findings of this study are available within the article.

APPENDIX: DELAYED PROPER ORTHOGONAL DECOMPOSITION

Let $\boldsymbol{q}(t)$ denote the flow field, and $\boldsymbol{q}'(t)$ denotes the mean-subtracting snapshot of flow field. Delay embedding lifts a time series signal into a higher dimensional space by stacking it with time-shifted copies of itself. For the snapshot of flow field $\boldsymbol{q}'(t)$, the lifted Hankel matrix $\boldsymbol{Q}$ is obtained as follows:

$$\mathbf{Q} = \begin{bmatrix} u(t_0) & u(t_1) & \cdots & u(t_{m-d}) \\ u(t_1) & u(t_2) & \cdots & u(t_{m-d-1}) \\ \vdots & \vdots & \ddots & \vdots \\ u(t_d) & u(t_{d+1}) & \cdots & u(t_m) \end{bmatrix}. \tag{A1}$$

The matrix $\boldsymbol{Q} \in R^{\mathrm{N}\times(\mathrm{m}-\mathrm{d}+1)}$ contains d shifted copies of the original signal $\boldsymbol{q}'$, each offset from the last by one time step, where $N = d \times n$. The delay embedding number d determines the dimension of the delay coordinate space into which the columns of $\boldsymbol{q}'$ are lifted. Although the embeddings d does not carry with it any risk of causing the model regression to be underdetermined, it highly

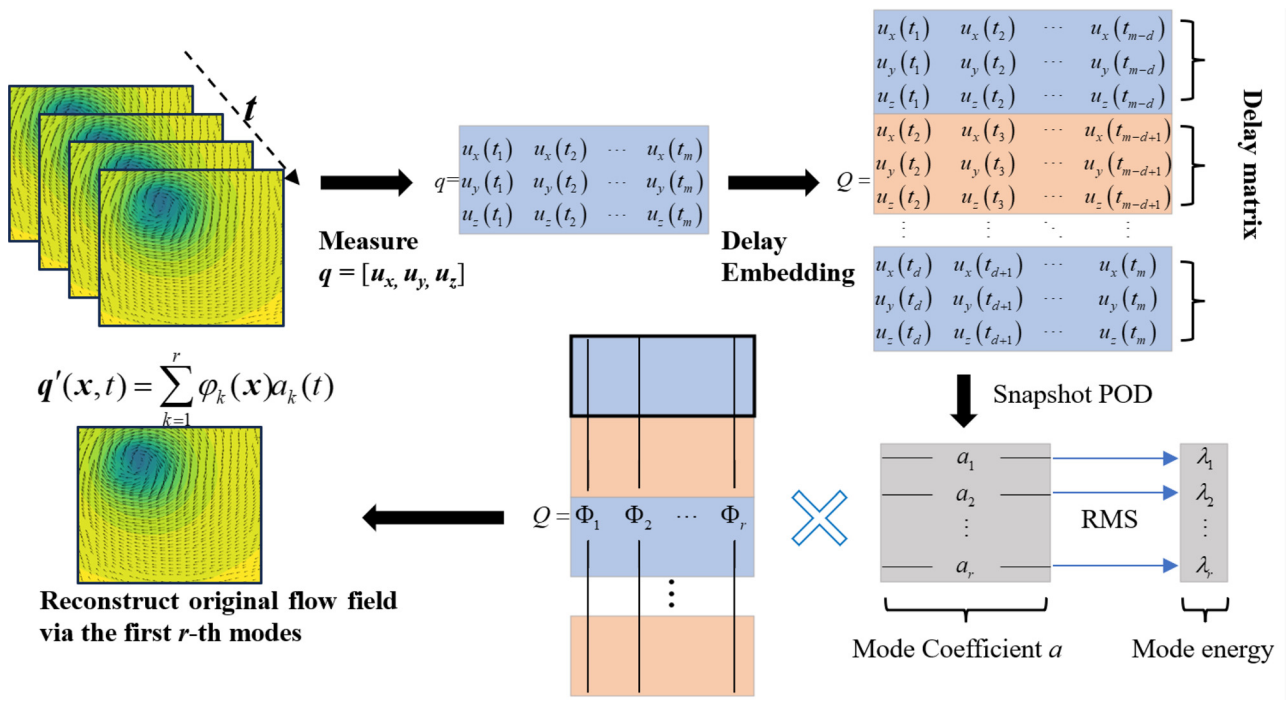

FIG. 21. Description of delay-embedded POD and flow field reconstruction.

influences on the characteristic of the mode coefficients. The quantitative analysis of delay embedding number can be found in Sec. IV.

For the $\mathbf{q}'(\mathbf{x}, t)$ at the time t, it can be decomposed into a finite sum of spatial eigenfunctions $\boldsymbol{\phi}_k(\boldsymbol{x})$ multiplied by a temporal modal coefficient $a_k(t)$,

$$\mathbf{q}'(\mathbf{x}, t) = \sum_{k=1}^{N} \boldsymbol{\Phi}_k(\mathbf{x}) a_k(t). \tag{A2}$$

Here, $\boldsymbol{\Phi}_k(\boldsymbol{x})$ satisfy the orthonormality condition, i.e., $\boldsymbol{\phi}_k \bullet \boldsymbol{\phi}_j = 0$ if $k \neq j$. The POD modes and corresponding temporal modal coefficients can be gained by the following procedures. First, original flow field data $\boldsymbol{q}$ are gathered into a matrix $\boldsymbol{Q}$ shown in the following equation:

$$\mathbf{Q} = [\mathbf{q}(t_1), \mathbf{q}(t_2), \ldots, \mathbf{q}(t_m)]. \tag{A3}$$

Here, m denotes the number of snapshots. Generally, in numerical simulation, the space dimension is always much larger than the snapshots. In this case, the snapshot POD method has the advantages of computationally more tractable eigenvalue problems than the traditional counterparts. The snapshot POD method is applied to solve the eigenvalue problem in the following equation:

$$\mathbf{Q}^T \mathbf{Q} \boldsymbol{\psi}_j = \lambda_j \boldsymbol{\psi}_j. \tag{A4}$$

Then the jth POD mode can be recovered from

$$\phi_j = \mathbf{Q} \psi_j / \sqrt{\lambda_j}. \tag{A5}$$

Due to the orthonormality condition of POD modes, the time-dependent mode coefficients $a_j(t)$ can be obtained by

$$a_j(t) = \frac{\langle \mathbf{q}(t), \phi_j \rangle}{\langle \phi_j, \phi_j \rangle}. \tag{A6}$$

Here, the angle brackets $\langle \bullet \rangle$ represent the inner product.

The original flow field at time t can be reconstructed by the first rth modes:

$$\mathbf{q}(\mathbf{x}, t) = \sum_{k=0}^{r} \varphi_k(\mathbf{x}) a_k(t), \tag{A7}$$

where φ_k is the vector composed of the first nth elements of $\boldsymbol{\phi}_k$. Note that when $k = 0$, $a_0 = 1.0$ and Φ_0 is the time-average flow field. The flow chart of delayed POD preprocessing and reconstruction of wake is presented in Fig. 21.

REFERENCES

Ashrafi, A., Romanic, D., Kassab, A., Hangan, H., and Ezami, N., "Experimental investigation of large-scale tornado-like vortices," J. Wind Eng. Ind Aerodyn. **208**, 104449 (2021).

Atam, E., Mathelin, L., and Cordier, L., "Identification-based closed-loop control strategies for a cylinder wake flow," IEEE Trans. Control Syst. Technol. **25**(4), 1488–1495 (2017).

Baker, C. and Sterling, M., "Are tornado vortex generators fit for purpose?," J. Wind Eng. Ind. Aerodyn. **190**, 287–292 (2019).

Begiashvili, B., Groun, N., Garicano-Mena, J., Le Clainche, S., and Valero, E., "Data-driven modal decomposition methods as feature detection techniques for flow problems: A critical assessment," Phys. Fluids **35**(4), 041301 (2023).

Buccino, G., "Full order and reduced order models for the Navier–Stokes equations in stream function-vorticity formulation," Master thesis (Politechnico, 2022).

Cao, S., Wang, J., Cao, J., Zhao, L., and Chen, X., "Experimental study of wind pressures acting on a cooling tower exposed to stationary tornado-like vortices," J. Wind Eng. Ind. Aerod. **145**, 75–86 (2015).

Cao, Y. and Liu, Z., "Study of wandering motion effects on the tornado-borne debris using proposed simplified numerical models," J. Wind Eng. Ind Aerodyn. **233**, 105318 (2023).

Chang, Y.-H., Wang, X., Zhang, L., Li, Y., Mak, S., Wu, C.-F. J., and Yang, V., "Reduced-order modeling for complex flow emulation by common kernel-smoothed proper orthogonal decomposition," AIAA J. **59**(9), 3291–3303 (2021).

Celik, I. B., Cehreli, Z. N., and Yavuz, I., "Index of resolution quality for large eddy simulations," J. Fluids Eng. Trans. ASME **127**(5), 949–958 (2005).

Chen, G. and Lombardo, F. T., "An analytical pattern-based method for estimation of a near-surface tornadic wind field," J. Wind Eng. Ind Aerodyn. **194**, 103999 (2019).

Das, S., and Giannakis, D., "Delay-coordinate maps and the spectra of Koopman operators," J. Stat. Phys. **175**(6), 1107–1145 (2019).

Davies-Jones, R., "A review of supercell and tornado dynamics," Atmos. Res. **158–159**, 274–291 (2015).

De Cillis, G., Cherubini, S., Semeraro, O., Leonardi, S., and De Palma, P., "POD-based analysis of a wind turbine wake under the influence of tower and nacelle," Wind Energy **24**(6), 609–633 (2021).

Ding, H., Li, W., and Qiao, J., "A self-organizing recurrent fuzzy neural network based on multivariate time series analysis," Neural Comput. Appl. **33**(10), 5089–5109 (2021).

Dylewsky, D., Kaiser, E., Brunton, S. L., and Kutz, J. N., "Principal component trajectories for modeling spectrally continuous dynamics as forced linear systems," Phys. Rev. E **105**(1), 015312 (2022).

Gairola, A. and Bitsuamlak, G., "Numerical tornado modeling for common interpretation of experimental simulators," J. Wind Eng. Ind Aerodyn. **186**, 32–48 (2019).

Gillmeier, S., Sterling, M., Hemida, H., and Baker, C. J., "A reflection on analytical tornado-like vortex flow field models," J. Wind Eng. Ind Aerodyn. **174**, 10–27 (2018).

Gunár, S., Labrosse, N., Luna, M., Schmieder, B., Heinzel, P., Kucera, T. A., Levens, P. J., López Ariste, A., Mackay, D. H., and Zapiór, M., "On the physical nature of the so-called prominence tornadoes," Space Sci. Rev. **219**(4), 33 (2023).

Haan, F. L., Jr., Sarkar, P. P., and Gallus, W. A., "Design, construction and performance of a large tornado simulator for wind engineering applications," Eng. Struct. **30**(4), 1146–1159 (2008).

Honerkamp, R., Yan, G., and Snyder, J. C., "A review of the characteristics of tornadic wind fields through observations and simulations," J. Wind Eng. Ind Aerodyn. **202**, 104195 (2020).

Huo, S., Hemida, H., and Sterling, M., "Numerical study of debris flight in a tornado-like vortex," J. Fluids Struct. **99**, 103134 (2020).

Karami, M., Carassale, L., and Hangan, H., "Statistical and modal analysis of surface pressure fluctuations in tornado-like vortices," Phys. Fluids **32**(7), 075109 (2020).

Karami, M., Hangan, H., Carassale, L., and Peerhossaini, H., "Coherent structures in tornado-like vortices," Phys. Fluids **31**(8), 085118 (2019).

Li, Z. and Wu, Q., *Research on Real-Time Correction of Flood Forecasts in the Middle Reaches of the Yellow River using AR, ARMAX and LSTM models* (Authorea, 2020).

Li, C. Y., Chen, Z., Zhang, X., Tim, K., and Lin, C., "Koopman analysis by the dynamic mode decomposition in wind engineering," J. Wind Eng. Ind Aerodyn. **232**, 105295 (2023).

Li, C. Y., Chen, Z., Tse, T. K., Weerasuriya, A. U., Zhang, X., Fu, Y., and Lin, X., "A parametric and feasibility study for data sampling of the dynamic mode decomposition: Range, resolution, and universal convergence states," Nonlinear Dyn. **107**(4), 3683–3707 (2022).

Liu, Z. and Ishihara, T., "Numerical study of turbulent flow fields and the similarity of tornado vortices using large-eddy simulations," J. Wind Eng. Ind Aerodyn. **145**, 42–60 (2015).

Luo, C., Tan, C., Wang, X., and Zheng, Y., "An evolving recurrent interval type-2 intuitionistic fuzzy neural network for online learning and time series prediction," Appl. Soft Comput. **78**, 150–163 (2019).
Matsui, M. and Tamura, Y., "Influence of swirl ratio and incident flow conditions on generation of tornado-like vortex," in *5th European and African Conference on Wind Engineering, Florence, Italy, 19–23 July 2009* (Firenze University Press, 2009), pp. 213–216.
Mendez, M., Balabane, M., and Buchlin, J.-M., "Multi-scale proper orthogonal decomposition of complex fluid flows," J. Fluid Mech. **870**, 988–1036 (2019).
Moon, J. S. and Manuel, L., "Toward understanding waked flow fields behind a wind turbine using proper orthogonal decomposition," J. Renewable Sustainable Energy **13**(2), 023302 (2021).
Nasiri, H. and Ebadzadeh, M. M., "MFRFNN: Multi-functional recurrent fuzzy neural network for chaotic time series prediction," Neurocomputing **507**, 292–310 (2022).
Ooi, C., Le, Q. T., Dao, M. H., Nguyen, V. B., Nguyen, H. H., and Ba, T., "Modeling transient fluid simulations with proper orthogonal decomposition and machine learning," Int. J. Numer. Methods Fluids **93**(2), 396–410 (2021).
Raj, N. A., Tafti, D., and Muralidhar, N., "Comparison of reduced order models based on dynamic mode decomposition and deep learning for predicting chaotic flow in a random arrangement of cylinders," Phys. Fluids **35**(7), 073330 (2023).
Refan, M. and Hangan, H., "Characterization of tornado-like flow fields in a new model scale wind testing chamber," J. Wind Eng. Ind Aerodyn. **151**, 107–121 (2016).
Refan, M. and Hangan, H., "Near surface experimental exploration of tornado vortices," J. Wind Eng. Ind Aerodyn. **175**, 120–135 (2018).
Rodríguez, O., Bech, J., Arús, J., Castán, S., Figuerola, F., and Rigo, T., "An overview of tornado and waterspout events in Catalonia (2000–2019)," Atmos. Res. **250**, 105415 (2021).
Romanic, D., Refan, M., Wu, C.-H., and Michel, G., "Oklahoma tornado risk and variability: A statistical model," Int. J. Disaster Risk Reduct. **16**, 19–32 (2016).
Sobash, R. A., Romine, G. S., Schwartz, C. S., Gagne, D. J., and Weisman, M. L., "Explicit forecasts of low-level rotation from convection-allowing models for next-day tornado prediction," Weather Forecasting **31**(5), 1591–1614 (2016).
Standohar-Alfano, C. D., van de Lindt, J. W., and Ellingwood, B. R., "Vertical load path failure risk analysis of residential wood-frame construction in tornadoes," J. Struct. Eng. **143**(7), 04017045 (2017).
Taira, K., Brunton, S. L., Dawson, S. T., Rowley, C. W., Colonius, T., McKeon, B. J., Schmidt, O. T., Gordeyev, S., Theofilis, V., and Ukeiley, L. S., "Modal analysis of fluid flows: An overview," AIAA J. **55**(12), 4013–4041 (2017).
Tang, Z., Feng, C., Wu, L., Zuo, D., and James, D. L., "Characteristics of tornado-like vortices simulated in a large-scale ward-type simulator," Boundary Layer Meteorol. **166**, 327–350 (2018).
Tochimoto, E., "Environmental controls on tornadoes and tornado outbreaks," Atmos. Ocean **60**(3–4), 399–421 (2022).
Verma, S. and Selvam, R. P., "CFD model validation with experimental tornado wind field & comparison of wind field in different tornado chambers," Wind Struct. **33**(5), 367 (2021).
Wang, J., Cao, S., Pang, W., and Cao, J., "Experimental study on effects of ground roughness on flow characteristics of tornado-like vortices," Boundary Layer Meteorol. **162**, 319–339 (2017).
Wang, M., Cao, S., and Cao, J., "POD-based analysis of time-resolved tornado-like vortices," Wind Struct. **33**(1), 13–27 (2021).
Wang, M., Cao, S., and Cao, J., "Numerical study on applicability of various swirl ratio definitions to characterization of tornado-like vortex flow field," J. Wind Eng. Ind Aerodyn. **220**, 104841 (2022).
Ward, N. B., "The exploration of certain features of tornado dynamics using a laboratory model," J. Atmos. Sci. **29**(6), 1194–1204 (1972).
Womble, J. A., Wood, R. L., and Mohammadi, M. E., "Multi-scale remote sensing of tornado effects," Front. Built Environ. **4**, 66 (2018).
Wu, Z., Laurence, D., Utyuzhnikov, S., and Afgan, I., "Proper orthogonal decomposition and dynamic mode decomposition of jet in channel crossflow," Nucl. Eng. Des. **344**, 54–68 (2019).
Xu, F., Ma, J., Chen, W.-L., Xiao, Y.-Q., and Duan, Z.-D., "Analysis of load characteristics and responses of low-rise building under tornado," Procedia Eng. **210**, 165–172 (2017).
Zancanaro, M., Stabile, G., and Rozza, G., "A segregated reduced order model of a pressure-based solver for turbulent compressible flows," arXiv:2205.09396 (2022).
Zhang, D., Liu, B., Liang, Y., Jiang, W., Gao, H., Zhang, J., and Hu, G., "Numerical study of dynamic amplification factor and characteristic wind curves of high-speed train in tornado-like vortices," J. Wind Eng. Ind Aerodyn. **247**, 105707 (2024).
Zhang, H., Wang, H., Xu, Z., Liu, Z., and Khoo, B. C., "Investigation of the fluctuating velocity in a single-cell tornado-like vortex based on coherent structure extraction," Phys. Fluids **35**(1), 015135 (2023).
Zhang, Z. Z., Pan, H. R., and Zhu, Y. Q., "Automated modeling of nonlinear systems using fuzzy modular neural network," J. Intell. Fuzzy Syst. **46**, 3605–3617 (2024).
Zhou, L., Wen, J., Wang, Z., Deng, P., and Zhang, H., "High-fidelity wind turbine wake velocity prediction by surrogate model based on d-POD and LSTM," Energy **275**, 127525 (2023).
Zhu, Q., Li, H., Zhu, H., Zhou, L., Tse, K. T., and Zhang, H., "Koopman mode analysis on discovering distributed energy transfer of post-transient flutter of a bluff body," Ocean Eng. **309**, 118557 (2024a).
Zhu, Q., Zhou, L., Zhang, H., Tse, K. T., Tang, H., and Noack, B. R., "A zero-net-mass-flux wake stabilization method for blunt bodies via global linear instability," Phys. Fluids **36**(4), 043617 (2024b).
Zhu, Q., Zhou, L., Tse, K. T., Ning, X., and Zhang, H., "Aerodynamic interference effects of bridge-train-like bluff bodies with small flow attack angle," Phys. Fluids **36**(9), 093621 (2024c).